Research Article

ADVANCED PHOTONICS

Iso-propagation vortices with OAM-independent size and divergence toward future faster optical communications

Wenxiang Yan,[a,b] Zhaozhong Chen,[c] Xian Long,[a,b] Yuan Gao,[a,b] Zheng Yuan,[a,b] Zhi-Cheng Ren,[a,b] Xi-Lin Wang,[a,b] Jianping Ding,[a,b,d,*] and Hui-Tian Wang[a,b,*]

[a]Nanjing University, School of Physics, National Laboratory of Solid State Microstructures, Nanjing, China
[b]Nanjing University, Collaborative Innovation Center of Advanced Microstructures, Nanjing, China
[c]University of Glasgow, James Watt School of Engineering, Glasgow, United Kingdom
[d]Nanjing University, Collaborative Innovation Center of Solid-State Lighting and Energy-Saving Electronics, Nanjing, China

Abstract. Recognized in the 1990s, vortex beams' ability to carry orbital angular momentum (OAM) has significantly contributed to applications in optical manipulation and high-dimensional classical and quantum information communication. However, inherent diffraction in free space results in the inevitable expansion of beam size and divergence contingent upon the OAM, limiting vortex beams' applicability in areas such as spatial mode multiplexing communication, fiber-optic data transmission, and particle manipulation. These domains necessitate vortex beams with OAM-independent propagation characteristics. We introduce iso-propagation vortices (IPVs), vortex beams characterized by OAM-independent propagation behavior, achieved through precise radial index configuration of Laguerre–Gaussian beams. IPVs display notable transmission dynamics, including a reduced quality factor, resilience post-damage, and decreased and uniform modal scattering under atmospheric turbulence. Their distinctive attributes render IPVs valuable for potential applications in imaging, microscopy, optical communication, metrology, quantum information processing, and light–matter interactions. Notably, within optical communication, the case study suggests that the IPV basis, due to its OAM-independent propagation behavior, provides access to a more extensive spectrum of data channels compared with conventional spatial multiplexing techniques, consequently augmenting information capacity.

Keywords: orbital angular momentum; optical communication; structured light; optical vortices.

Received Dec. 20, 2023; revised manuscript received Apr. 2, 2024; accepted for publication Apr. 24, 2024; published online May 17, 2024; corrected Jul. 23, 2024.

[DOI: 10.1117/1.AP.6.3.036002]

1 Introduction

Vortices are a widespread phenomenon in nature, appearing in diverse forms such as quantum vortices in liquid nitrogen, typhoon vortices, and spiral galaxies in the Milky Way, observable both in macroscopic matter and structured electromagnetic fields. As delineated by Allen et al.[1] in 1992, vortex fields have become a focal point of research in light fields due to their capability to carry orbital angular momentum (OAM). This property has garnered substantial interest across various sectors, encompassing high-dimensional classical and quantum information communications,[2–4] micro-particle manipulation,[5,6] optical measurements,[7,8] optical imaging,[9,10] and processing.[11–13] A persistent challenge encountered is light diffraction, which results in increased beam size and divergence as the mode index augments. This also makes it difficult to control the size of vortex beams with respect to the variation of the OAM index. We elucidate this phenomenon in Figs. 1(a) and 1(b) using prominent OAM beams, specifically a subset of Laguerre–Gaussian (LG) beams with a null radial index (i.e., $p = 0$ for an $\mathrm{LG}_{l,p}$, where l and p denote the azimuthal and radial indices,

*Address all correspondence to Jianping Ding, jpding@nju.edu.cn; Hui-Tian Wang, htwang@nju.edu.cn

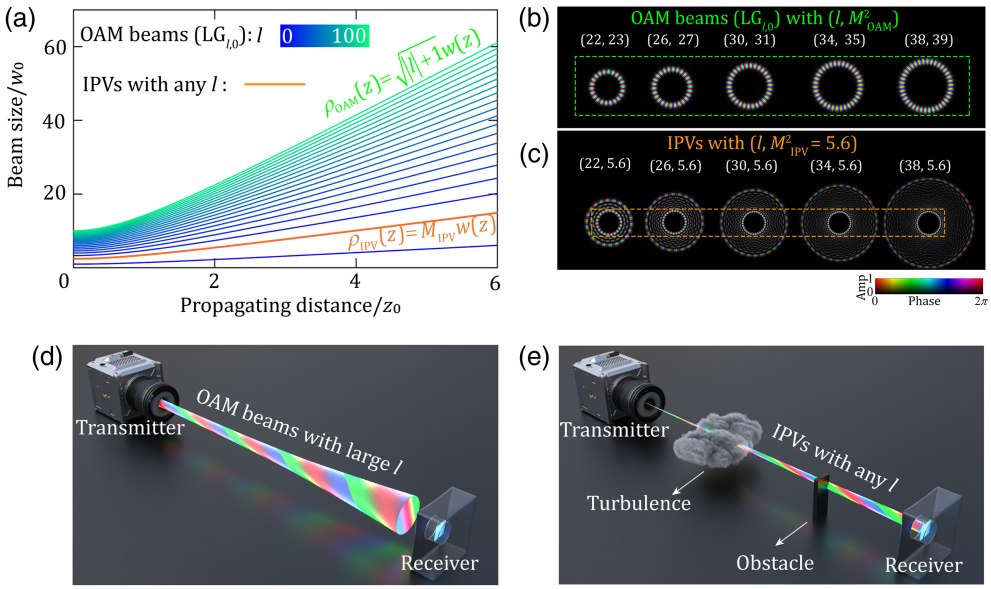

Fig. 1 Exploration of conventional OAM beams versus IPVs. (a) Traditional OAM beams (LG$_{l,0}$) showcase OAM-dependent size and divergence, with each color representing a unique OAM order l. Conversely, IPVs manifest OAM-independent size and divergence (the orange curve), whereas M_{IPV} is directly derived from the square root of the selected M^2_{IPV}. (b), (c) Complex field patterns for OAM beams (LG$_{l,0}$) and IPVs with identical beam waist but varying OAM orders. M^2_{IPV} and M^2_{OAM} are the quality factors of IPVs and OAM beams (LG$_{l,0}$). (d) Receivers with limited size obstruct the passage of OAM beams having large l values due to increasing beam size and divergence as the mode index grows.[14] However, (e) IPVs of any l can easily traverse because of their OAM-independent propagation characteristics, maintaining their structure even after turbulence or obstacles.[14]

respectively). This intrinsic diffraction-caused, OAM-dependent propagation behavior limits the expansive applications of vortex fields. In the context of optical communication, the behavior that the beam size and divergence of vortex beams increase with OAM necessitates larger receivers for more modes and greater capacity, posing a constraint of the feasible capacity for spatial multiplexing especially with realistically limited-size receivers,[15–18] as depicted in Fig. 1(d). While there have been endeavors to overcome this limitation, conventional "perfect" vortex fields maintain OAM-independent size predominantly near a focal plane and undergo degradation due to OAM-dependent divergence,[19,20] as displayed in Figs. 2(a)–2(f). To our knowledge, vortex beams exhibiting OAM-independent size and divergence have not been reported.

In our research, we discerned that the innermost rings of LG beams display distinct dynamic transmission properties: they possess a markedly small size and divergence, both of which can remain OAM-independent during propagation with precise radial index configuration. These innermost rings, demonstrating OAM-independent propagation, are hereby termed iso-propagation vortices (IPVs). Due to their reduced and OAM-independent size and divergence, IPVs undergo decreased and more consistent modal scattering in atmospheric turbulence. IPVs also retain their structure post-damage. Their unique attributes render IPVs instrumental for potential applications in imaging, microscopy, optical communication, metrology, quantum information processing, and light–matter interactions. For instance, within the domain of optical communication, the case study indicates that the IPV basis, endowed with OAM-independent propagation, enables access to a more expansive array of data channels compared with traditional spatial multiplexing techniques, thus augmenting information capacity, as delineated in Fig. 1(e).

2 Result

2.1 IPVs with OAM-Independent Size and Divergence

The complex amplitude distribution of a normalized LG beam carrying OAM of $l\hbar$ per photon in the cylindrical coordinate system (r, φ, z) is represented by[21]

$$\begin{aligned}\mathrm{LG}_{l,p}(r,\varphi,z) &= \sqrt{\frac{2p!}{\pi(|l|+p)!}}\frac{1}{w(z)}\left[\frac{\sqrt{2}r}{w(z)}\right]^{|l|}L_p^{|l|}\left[\frac{2r^2}{w^2(z)}\right]\exp\left[-\frac{r^2}{w^2(z)}\right] \\ &\quad\times\exp\left[ikz+ik\frac{r^2}{2R(z)}+il\varphi-i(|l|+2p+1)\zeta(z)\right], \quad (1)\end{aligned}$$

where $L_p^{|l|}$ denotes the Laguerre polynomial with the azimuthal index l (or topological charge) and the radial index p, $k=2\pi/\lambda$ is the wavenumber with λ being the wavelength, and

$$\begin{aligned}w(z) &= w_0\sqrt{1+\left(\frac{z}{z_0}\right)^2}, \quad R(z)=z\left[1+\left(\frac{z_0}{z}\right)^2\right], \\ \zeta(z) &= \arctan\left(\frac{z}{z_0}\right), \quad z_0=\frac{\pi w_0^2}{\lambda}, \quad w_0=\sqrt{\frac{\lambda z_0}{\pi}}, \quad (2)\end{aligned}$$

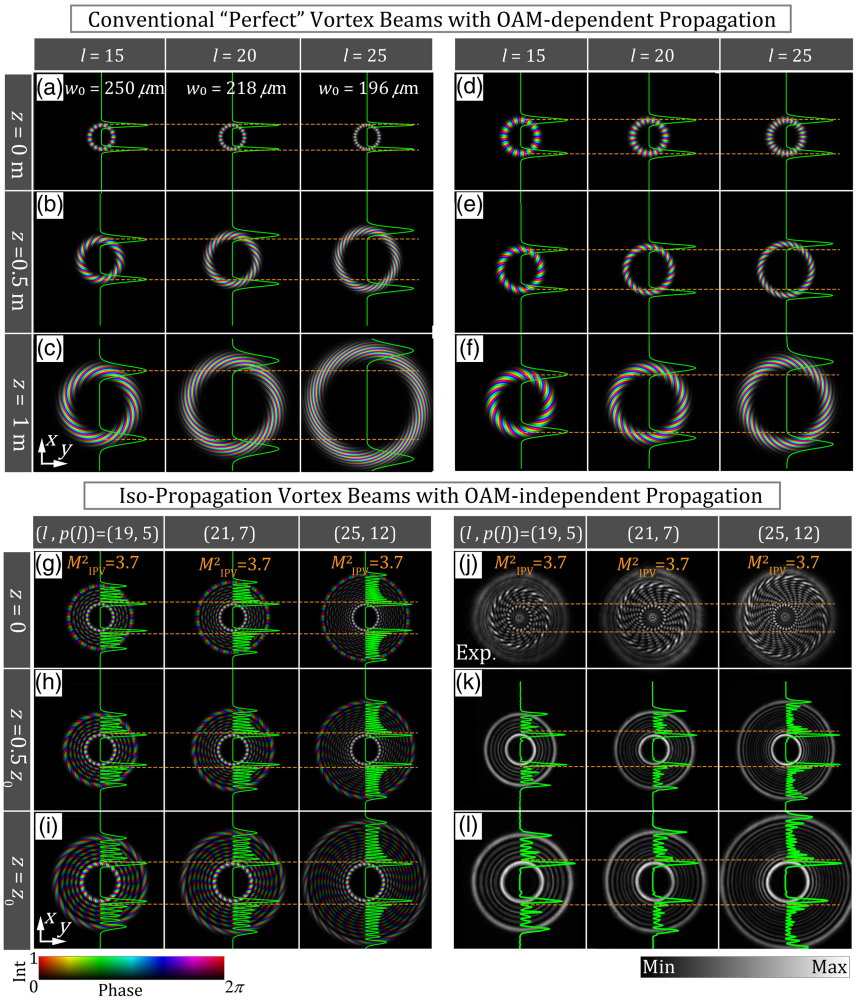

Fig. 2 Demonstration of OAM-dependent and OAM-independent propagation. The complex amplitude distributions of (a)–(c) "Perfect Laguerre–Gauss beams" (Ref. 19) and (d)–(f) "Perfect vortex beam" (Ref. 20) at $z = 0$, 0.5, and 1 m, respectively. w_0, the beam waist at $z = 0$. (g)–(i) The complex amplitude distributions of the innermost-ring-based IPVs with global $M^2_{\mathrm{IPV}} = 3.7$ at $z = 0$, $0.5z_0$, and z_0, respectively. (j)–(l) The corresponding experimental results for panels (g)–(i); especially, (j) is the interference patterns between the IPVs and a reference plane wave. The luminance and color of the color map refer to the intensity (Int) and phase, respectively; the green curves represent intensity profiles along the x axis, and the horizontal orange dashed lines serve as a reference for indicating the size of the vortex rings. For further experimental details, refer to Sec. 5 of the Supplementary Material.

with w_0 denoting the beam waist at $z = 0$. The root-mean-squared waist radius (which defines the size of the LG beam) $\rho_{\mathrm{LG}}(z) = \sqrt{|l| + 2p + 1}w(z)$ and divergence angle $\theta_{\mathrm{LG}} = \lim_{z\to\infty} \mathrm{d}\rho_{\mathrm{LG}}(z)/\mathrm{d}z = \sqrt{|l| + 2p + 1}\theta_0$ describe the free-space propagation property of the LG beam and are vital for the free-space optical (FSO) communication,[22] where θ_0 is the divergence angle of the fundamental Gaussian beam. The beam quality factor (M^2),[23] defined as the ratio between the space–bandwidth products of the LG beam, $\rho_{\mathrm{LG}}(0)\theta_{\mathrm{LG}}$, and of the fundamental Gaussian beam, $w_0\theta_0$, characterizes the propagation dynamics based on the inherent uncertainty principle between the beam size and divergence,[24]

$$M^2_{\mathrm{LG}}(l, p) = \frac{\rho_{\mathrm{LG}}(0)\theta_{\mathrm{LG}}}{w_0\theta_0} = |l| + 2p + 1. \tag{3}$$

From the relation $\rho_{\mathrm{LG}}(z) = M_{\mathrm{LG}}(l, p)w(z)$ and $\theta_{\mathrm{LG}} = M_{\mathrm{LG}}(l, p)\theta_0$, we find an important characteristic: different LG beams with the same M^2_{LG} always hold the same size and the same divergence upon propagating; that is, they retain the same propagation dynamics. In addition, in most OAM-interplaying systems, OAM or vortex beams are rendered by $\mathrm{LG}_{l,0}(r, \varphi, z)$, i.e., a subset of LG beams with $p = 0$, whose beam size $\rho_{\mathrm{OAM}}(z) = \sqrt{|l| + 1}w(z)$ [illustrated in Fig. 1(a)] and quality factor $M^2_{\mathrm{OAM}}(l) = |l| + 1$ are both the smallest for each beam with OAM of $l\hbar$ per photon.

After analyzing Eq. (1), we have derived the following analytical expression for the innermost ring size of the LG beam (i.e., the radius of the brightest ring, instead of the root-mean-squared waist radius; see Sec. 1 of the Supplementary Material for details):

$$\rho_{\mathrm{IR}}(z) \approx \frac{|l|+2}{2\sqrt{|l|+2p+1}} w(z). \tag{4}$$

The subscript "IR" denotes the parameters related to the innermost ring for brevity. The divergence angle is given by

$$\theta_{\mathrm{IR}} \approx \lim_{z\to\infty} \mathrm{d}\rho_{\mathrm{IR}}(z)/\mathrm{d}z = \frac{|l|+2}{2\sqrt{|l|+2p+1}} \theta_0. \tag{5}$$

Consequently, the "quality factor" defined by the innermost ring can be written as

$$M^2_{\mathrm{IR}}(l,p) \approx \frac{\rho_{\mathrm{IR}}(0)\theta_{\mathrm{IR}}}{w_0\theta_0} = \frac{(|l|+2)^2}{4(|l|+2p+1)}. \tag{6}$$

Given a global quality factor as $M^2_{\mathrm{IR}}(l) = M^2_{\mathrm{IPV}}$, the radial index of beams can be determined by $p(l) = \mathrm{round}[(0.5|l|+1)^2/2M^2_{\mathrm{IPV}} - 0.5(|l|+1)]$, with the round$(\cdot)$ function indicating rounding to the nearest integer. As per Eqs. (4)–(6), this set of innermost rings, characterized by the global parameter M^2_{IPV}, exhibits an OAM-independent size, given by $\rho_{\mathrm{IPV}}(z) = M_{\mathrm{IPV}} w(z)$, and also an OAM-independent divergence, denoted by $\theta_{\mathrm{IPV}} = M_{\mathrm{IPV}}\theta_0$. Consequently, these rings demonstrate OAM-independent propagation behavior, as depicted in Figs. 2(g)–2(l), and are donated as IPVs. By contrast, conventional "perfect" vortices, which show OAM-independent radii only near a specific plane (usually the focal plane), fail to maintain OAM-independent propagation because of OAM-dependent divergence. Specifically, perfect Laguerre–Gauss beams[19] compensate for the OAM-related expansion of beam size at a certain plane (e.g., $z = 0$ m) by adjusting the beam waist (w_0). However, these result in OAM-dependent divergence due to the variation in beam waist, as depicted in Figs. 2(a)–2(c). Similarly, a common form of perfect vortex beam,[20] generated by Fourier transforming Bessel–Gauss beams, exhibits OAM-independent radii solely in the focal plane ($z = 0$ m). Yet, it also cannot sustain OAM-independent propagation owing to OAM-dependent divergence, as shown in Figs. 2(d)–2(f).

2.2 Transmission Characteristics of IPVs

2.2.1 Superior transmission dynamics

Equations (4)–(6) indicate that the IPV mode parameters (M^2, ρ, θ) exhibit an increase with the absolute value of topological charge ($|l|$) while showing a decrease with the radial index (p). This behavior contrasts with LG beams, where these parameters augment with both $|l|$ and p. As a result, for a given topological charge l, IPVs display significantly lower values of parameters (M^2, ρ, θ) compared with conventional LG beams. In Figs. 3(a)–3(d), we contrast M^2 values for LG beams $[M^2_{\mathrm{LG}}(l,p)]$ with those for IPV $[M^2_{\mathrm{IPV}}(l,p)]$ across the initial 10,000 orders. This comparison highlights a wider dispersion range for $M^2_{\mathrm{LG}}(l,p)$, spanning 0 to 300, in contrast to $M^2_{\mathrm{IPV}}(l,p)$, which primarily ranges between 0 and 20. Consequently, IPVs demonstrate superior transmission properties, including reduced size, divergence, and enhanced quality factor, surpassing those of LG beams.

2.2.2 Self-restoration post-damage facilitated by sidelobes

Another noteworthy property of IPVs is their self-rehabilitation. Post severe damage, these vortices tend to regenerate their original form, bolstered by sidelobes. In Fig. 3(e), we present experimental evidence of an IPV encountering an obstruction (a square-shaped obstacle). The IPV gradually restores its original structure over a certain distance, thanks to the support from its sidelobes. This experimental result was obtained using the setup detailed in Ref. 26, as well as in Sec. 5 of the Supplementary Material. In addition, numerical simulations of the energy circulation within these vortices clarify how they recover. Figure 3(f) unveils that while the IPV's energy flow is strong in the azimuthal (circular) direction, the key to its regeneration lies predominantly in the radial (inward) component. This component draws energy from the outer sidelobes. In the absence of this "energy reserve" in sidelobes, the OAM beam's vortex ring fails to exhibit similar self-repair capabilities post-damage, as illustrated in Figs. 3(g) and 3(h). Such sidelobe-facilitated rejuvenation enhances the robustness of IPVs against disturbances, in contrast to OAM beams. To quantitatively describe the reconstruction of impaired IPVs in Figs. 3(e) and 3(f), we introduced the Pearson correlation coefficients (PCCs) between the intensity maps of IPVs at each z-axial location with and without the square obstacle. The PCCs of matrices X and Y are defined by $\mathrm{PCC}(X,Y) = \mathrm{cov}(X,Y)/\sigma_X\sigma_Y$, where $\mathrm{cov}(X,Y)$ is the covariance of X and Y and σ_X or σ_Y is the standard deviation of matrices X or Y.

2.2.3 Reduced modal scattering in atmospheric turbulence

Atmospheric turbulence, along with the diffraction-induced beam expansion, impedes the attainment of faster and more distant optical links.[27] Relevant studies showed that modal scattering exacerbates with escalating turbulence strength and beam size.[28] As depicted in Figs. 4(a)–4(d), in comparison with the LG beam, the IPV undergoes a relatively attenuated modal scattering effect due to atmospheric turbulence. Figures 4(g)–4(j) emphasize that, in contrast to traditional LG beams with OAM-dependent propagation dynamics, IPVs, which have OAM-independent characteristics and reduced beam size and lower divergence (e.g., $M^2_{\mathrm{IPV}} = 5.6$), encounter lesser and more uniform modal scattering across various mode orders. Therefore, IPVs stand out as promising candidates for future developments in atmospheric communication multiplexing.[29,30] More detailed analysis and discussion can be found in Sec. 2 of the Supplementary Material.

2.3 Case Study in Optical Communication with Enhanced Capacity

The pursuit of greater capacity for information capture and processing remains an essential objective among researchers in the field of optical communication.[31] Optical multiplexing, leveraging degrees of freedom such as polarization and wavelength, has historically augmented the capacity of both radio-frequency and optical communication systems.[32–34] Spatial mode-division multiplexing introduces a novel approach by utilizing orthogonal spatial modes as distinct communication channels.[35–40] To illustrate, consider an FSO link that integrates spatial mode-division multiplexing with Q orthogonal modes, polarization-division multiplexing with two distinct polarization states, and wavelength-division multiplexing with T wavelengths. When encoded with 100 Gbit/s quadrature phase-shift keying data, this configuration can achieve a collective capacity of $Q \times 2 \times T \times 100$ Gbit/s. This capacity can escalate to several Pbit/s,[38] offering the promise of advancing both deep-space and proximate Earth optical communications by

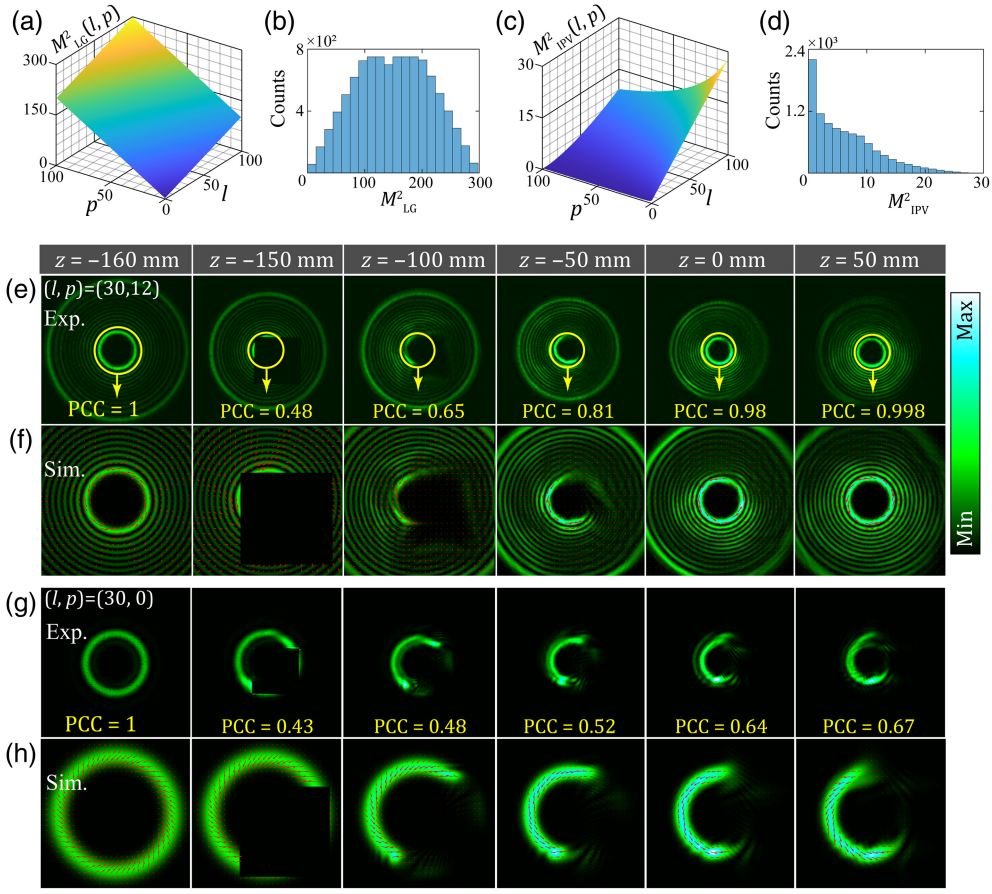

Fig. 3 Smaller quality factors and self-healing properties of IPVs. Quality factors of (a) LG beams-$M^2_{\mathrm{LG}}(l,p)$ and (c) IPVs-$M^2_{\mathrm{IPV}}(l,p)$ for 10,000 lowest orders (l and p equal 0,1, …, 99; results for $l<0$ are the same as those for $l>0$ and are omitted here). The corresponding distribution histograms are shown in panels (b) and (d). The IPV ($l=30$, $p=12$, $z_0=150$ mm) is blocked by a square obstacle at $z=-150$ mm: (e) experimental intensity maps at different z-axial locations (Video 1, MP4, 732 KB [URL: https://doi.org/10.1117/1.AP.6.3.036002.s1]); (f) transversal energy flow of panel (e), following from the cycle-average Poynting vector,[25] the red arrows indicate the value and direction of each flow (Video 2, MP4, 1.52 MB [URL: https://doi.org/10.1117/1.AP.6.3.036002.s2]), where PCC is PCC of innermost rings; panels (g) and (h) are the same as panels (e) and (f) but for OAM beams (i.e., $\mathrm{LG}_{l,0}$) (Video 3, MP4, 358 KB [URL: https://doi.org/10.1117/1.AP.6.3.036002.s3]; Video 4, MP4, 1.46 MB [URL: https://doi.org/10.1117/1.AP.6.3.036002.s4]). The sharp-edged square obstacle is produced as masks via the process of photoetching chrome patterns on a glass substrate. For further experimental details, refer to Sec. 5 of the Supplementary Material.

substantially elevating capacity and spectral efficiency. However, the prevailing implementation of spatial mode-division multiplexing encounters a formidable impediment.[15–18] Inherent diffraction causes an inevitable increase in beam size and divergence concomitant with the rising mode indices, including the OAM index in vortex beams. These result in a prerequisite for larger receivers to accommodate higher capacities involving more modes. This need frequently clashes with the practical size constraints of such receivers, critically curbing the capacity potential of contemporary spatial mode-division multiplexing, as delineated in Fig. 1(d).

Employing the IPV basis, given its OAM-independent propagation characteristics, avails access to an expanded suite of subchannels compared with conventional spatial multiplexing approaches, thus enhancing the information capacity for feasible free-space optical systems, as delineated in Fig. 1(e). To validate this, the number of IPVs suitable for a line-of-sight free-space communication system characterized by a space-bandwidth product (SBP) of $2R_0\times 2\mathrm{NA}/\lambda$ was determined, where R_0 and NA are the aperture radius and numerical aperture of both circular apertures of transmitter and receiver, and λ is the wavelength. Following the procedure of Ref. 41, the system quality factor, denoted as $S=\pi R_0\times \mathrm{NA}/\lambda$, which is a dimensionless parameter and is $\pi/4$ times the SBP, was ascertained. Only beams with a quality factor less than the system's S value can traverse this system. The solution count for $M^2\le S$ provides the system's Q value. For example, when employing the LG beam multiplexing as the information carrier, the addressable subchannels can be computed as $Q_{\mathrm{LG}}(S)\approx 0.5\mathrm{floor}[S](\mathrm{floor}[S]+1)$ by resolving $M^2_{\mathrm{LG}}(l,p)=|l|+2p+1\le S$. Analogously, the

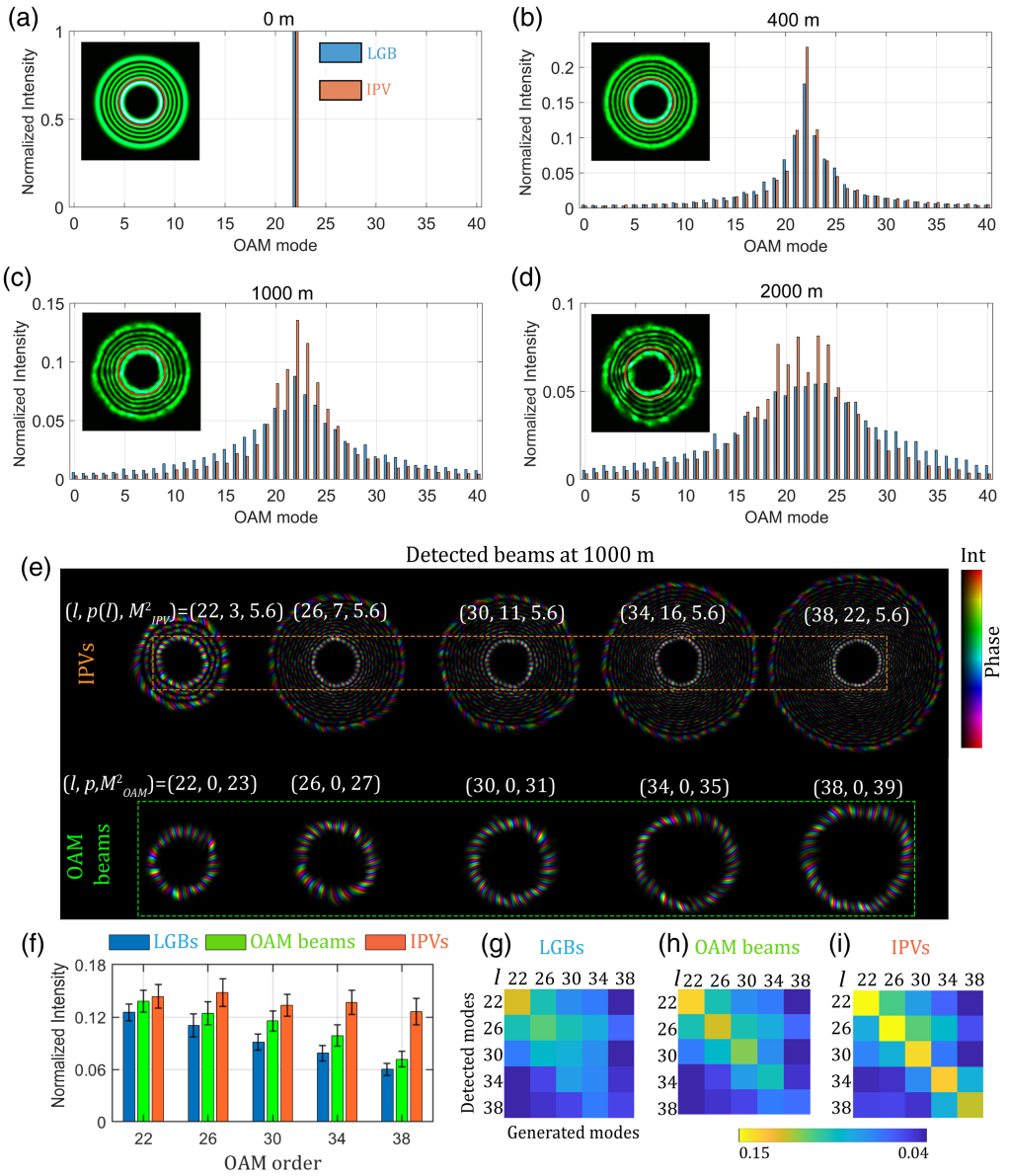

Fig. 4 Assessing free-space propagation amid atmospheric turbulence for the LG beam and corresponding innermost-ring-based IPV with $l = 22$ and $p = 5$ in panels (a)–(d) from 0 to 2000 m. The insets display the intensity patterns of the propagating LG beam at different distances, while the red circles represent the aperture to truncate the innermost ring. (e) The complex distributions for detected beams of IPVs with global $M^2_{\mathrm{IPV}} = 5.6$ and the corresponding OAM beams at $z = 1000$ m against atmospheric turbulence; (f) the normalized intensity in detected modes for each launched mode in panel (e) at $z = 1000$ m; (g)–(i) the cross talk matrices for LG beams, OAM beams, and IPVs.

numbers of addressable subchannels for conventional OAM beam multiplexing, Hermite–Gaussian beam multiplexing, and multi-input multi-output transmission are as follows: $Q_{\mathrm{OAM}}(S) \approx 2\mathrm{floor}[S] + 1$, $Q_{\mathrm{HG}}(S) = Q_{\mathrm{LG}} \approx 0.5\mathrm{floor}[S](\mathrm{floor}[S] + 1)$, and $Q_{\mathrm{MIMO}}(S) = \mathrm{round}[0.9S^2]$, respectively.[41]

M^2_{IPV} is set to be less than S, which ensures compatibility between IPVs with mode indices $[l, p(l)]$ and the FSO system characterized by the system quality factor S, resulting in a more substantial subchannel array. It is imperative to recognize that currently available spatial light modulators present constraints associated with panel and pixel dimensions, impacting the precise projection of structured beams with elevated mode orders. However, preliminary experiments (Sec. 3 of the Supplementary Material) incorporating 105 IPV subchannels (Video 5, MP4, 1.81 MB [URL: https://doi.org/10.1117/1.AP.6.3.036002.s5]) with $l = [-52, 52]$, $S = 6.25$, and $M^2_{\mathrm{IPV}} = 0.9S = 5.6$, manifest the pronounced enhancements of Q for IPV multiplexing compared with traditional methodologies. The demultiplexing intensity patterns in the preliminary experiments are shown in Video 6, MP4, 1.14 MB [URL: https://doi.org/10.1117/1.AP.6.3.036002.s6]. These enhancements range from 300% to 808%, in contrast to

$Q_{\mathrm{OAM}}(S=6.25)=13$, $Q_{\mathrm{LG}}(S=6.25)=Q_{\mathrm{HG}}(S=6.25)=21$, $Q_{\mathrm{MIMO}}(S=6.25)=35$. The number of IPV subchannels can be further boosted by the adoption of metasurface platforms with large panel sizes and ultrahigh resolution. When factoring in interchannel cross talk in mode-multiplexed communication, it is customary to select subchannels within specific mode intervals. Nevertheless, a higher subchannel limit (Q) for multiplexing corresponds to a greater number of practically applicable subchannels and enhanced capacity.

Figure 5 presents an illustrative example of this concept, showcasing an IPV-multiplexed transmission of Vincent van Gogh's iconic artwork "The Starry Night." This artwork, rendered in true color, was segmented into RGB layers. Each layer was encoded with 8-bit color depth; the color distribution histograms are presented in Fig. 5(b). The conveyed information per pixel was channeled via 24-bit IPV multiplexing, ensuring exceptional color fidelity. Bits 1 to 24 correspond to $l=[52,-50,48,-46,44,-42,40,-38,32,-30,28,-26,24,-22,20,-18,16,-14,12,-10,8,-6,4,-2]$ with $M^2_{\mathrm{IPV}}=5.6$. Upon receiving and decoding the high-density data streams of $128\times128\times24$ bits from the experimental setup of Sec. 3 of the Supplementary Material, we successfully recovered the true color image with an ultrahigh color fidelity. The error rate was impressively low at 2.45×10^{-4}, much lower than the forward error correction limit of 3.8×10^{-3}, as shown in Fig. 5(c). Figure 5(d) shows the color distribution histograms of this true-color image with 24 bits of color depth and the RGB layers with 8 bits of color depth. In this proof-of-principle experiment, the highest transmission rate reached $24\times11,000=0.264$ Mbit/s when using digital mirror devices at an 11 kHz refresh rate.

For a more comprehensive comparison of subchannels of different spatial multiplexing techniques, we calculated Q_{IPV} with different S using the empirical formula $Q_{\mathrm{IPV}}\approx2\mathrm{floor}[14.76S]+1$ [Emp. Q_{IPV}, the pink-dashed curve in Fig. 5(e)], which agrees well with the actual results (Q_{IPV}, the blue curve) in Fig. 5(e) (see details in Sec. 4 of the Supplementary Material). This approach attains an approximate 14-fold improvement for most systems compared with traditional OAM multiplexing of $Q_{\mathrm{OAM}}\approx2\mathrm{floor}[S]+1$. For practical FSO systems with limited-size receivers and $S<30$, IPV multiplexing offers more

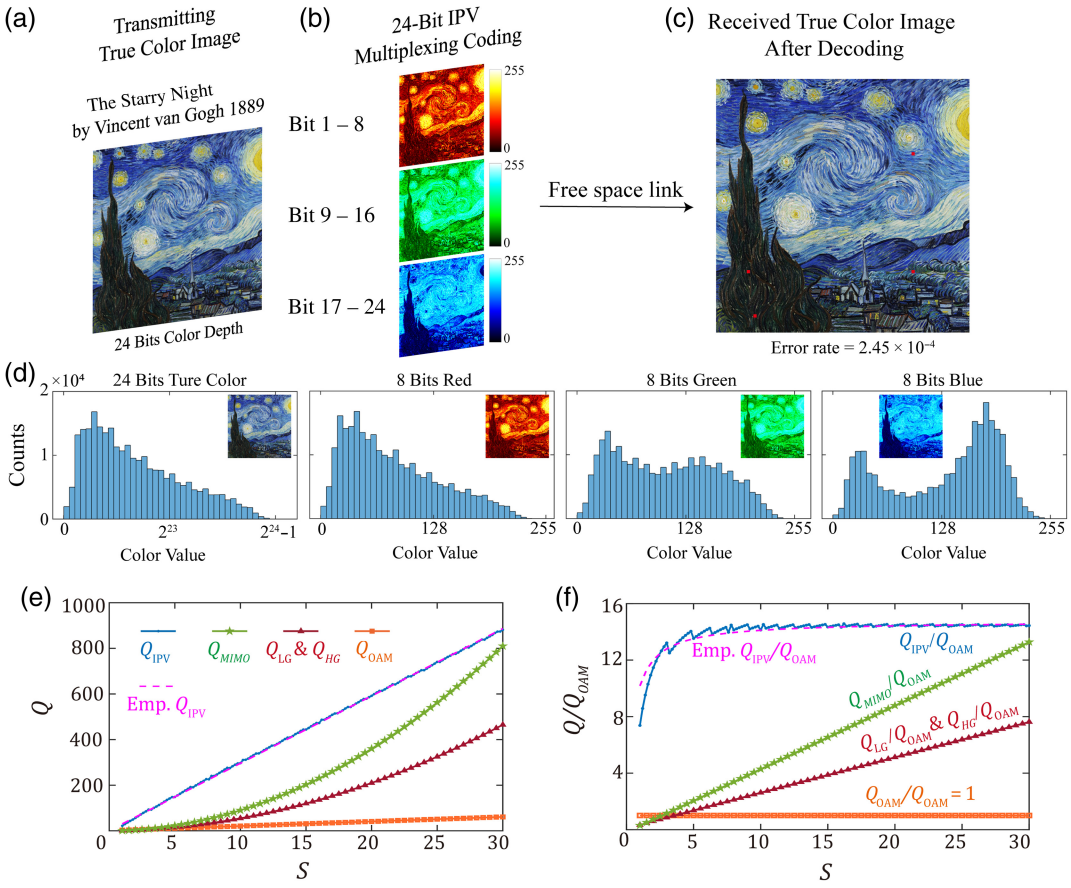

Fig. 5 Image transmission by 24-bit IPV multiplexing with ultrahigh color fidelity. (a) True color image, "The Starry Night" by Vincent van Gogh (1889), with 24 bits of color depth and 2^{24} colors including 128 pixels × 128 pixels, and (b) three RGB layers of panel (a) were encoded from bit 1 to 24; (c) received true color image after recovering with an error rate of 2.45×10^{-4}. (d) Color distribution histograms of the true color image with 24 bits of color depth and the RGB layers with 8 bits of color depth. The red pixels indicate the incorrect data received. (e) Numbers Q of independent spatial subchannels for spatial multiplexing techniques from $S=1$ to $S=30$; Emp., empirical. (f) The improvement of numbers of independent spatial subchannels in (e) versus Q_{OAM}.

subchannels than the spatial multiplexing technique,[37] such as LG beam multiplexing, HG beam multiplexing, and conventional multi-input multi-output (MIMO) transmission, as illustrated in Figs. 5(e) and 5(f). In comparison with the latest work on structured light, specifically multi-vortex geometric (MVG) beam multiplexing,[33] for the practical FSO systems with limited-size receivers and $S < 30$, Q_{MVG} for MVG beam multiplexing is close to Q_{LG} and thus also lower than Q_{IPV}. For instance, in the aforementioned preliminary experiments with given $S = 6.25$, the estimated $Q_{\mathrm{IPV}} = 185$ is in contrast to $Q_{\mathrm{OAM}} = 13$, $Q_{\mathrm{LG}}\,(Q_{\mathrm{HG}}) = 21$, and $Q_{\mathrm{MIMO}} = 35$.

3 Conclusion

In conclusion, the amplification of beam size and divergence due to diffraction-induced influences and the increase in mode indices (e.g., OAM) pose significant constraints on the applicability of vortex beams in areas such as spatial mode multiplexing communication, fiber-optic data transmission, and particle manipulation. The OAM-expansion propagation behavior, in particular, considerably restricts the feasible capacity for free-space optical links. In response to the need for vortex beams with OAM-independent propagation features, this study introduced IPVs, characterized by their OAM-independent size and divergence during propagation. Beyond iso-propagation with respect to OAM, IPVs exhibit distinctive transmission dynamics, including enhanced resilience post-damage, diminished quality factor, and reduced, uniform modal scattering under atmospheric disturbances. These properties position IPVs as potentially valuable tools for diverse applications. A comparison table among traditional vortex beams, perfect vortex beams, and IPV beams is shown in Table S2 in the Supplementary Material. In optical communication, for example, the IPV basis could expand available data channels, potentially surpassing traditional spatial multiplexing methods and thus boosting information capacity. In addition, the resilience of IPVs to damage and their consistent propagation characteristics may be beneficial in imaging and microscopy, possibly improving resolution and contrast. In quantum information processing, the ability of IPVs to maintain their structure post-damage and exhibit reduced modal scattering under atmospheric turbulence could be advantageous, although further research is needed to fully realize these applications. Similarly, the unique properties of IPVs might be exploited in studies of light–matter interactions, with potential applications in fields ranging from material science to optoelectronics. In summary, while the practical applications of IPVs hold promise, further research is necessary to fully understand their potential and to develop the technology for widespread use in various fields.

Disclosures

The authors declare no competing interests.

Code and Data Availability

All data that support the findings of this study are available within the article and Supplementary Information or from the corresponding author upon reasonable request.

Author Contributions

W.Y. and J.D. proposed the original idea and designed the study. W.Y. built the experimental system and performed the experiments. Z.C., X.L., Y.G., and Z.Y. assisted in the experiments. J.D. and H.T.W. supervised the project. All authors contributed in writing the paper.

Acknowledgments

This work was financially supported by the National Key Research and Development Program of China (Grant Nos. 2023YFA1406903 and 2022YFA1404800) and the National Natural Science Foundation of China (Grant Nos. 12374307, 12234009, and 12274215).

References

1. L. Allen et al., "Orbital angular momentum of light and the transformation of Laguerre–Gaussian laser modes," *Phys. Rev. A* **45**(11), 8185–8189 (1992).
2. J. Wang et al., "Tailoring light on three-dimensional photonic chips: a platform for versatile OAM mode optical interconnects," *Adv. Photonics* **5**(3), 036004 (2023).
3. A. Suprano et al., "Orbital angular momentum based intra and interparticle entangled states generated via a quantum dot source," *Adv. Photonics* **5**(4), 046008 (2023).
4. Q. Cao et al., "Propagation of transverse photonic orbital angular momentum through few-mode fiber," *Adv. Photonics* **5**(3), 036002 (2023).
5. E. Brasselet, "Torsion pendulum driven by the angular momentum of light: Beth's legacy continues," *Adv. Photonics* **5**(3), 034003 (2023).
6. J. Zhang et al., "Generation of time-varying orbital angular momentum beams with space-time-coding digital metasurface," *Adv. Photonics* **5**(3), 036001 (2023).
7. X. Li, Y. Tai, and Z. Nie, "Digital speckle correlation method based on phase vortices," *Opt. Eng.* **51**(7), 077004 (2012).
8. Z. Lin et al., "Single-shot Kramers–Kronig complex orbital angular momentum spectrum retrieval," *Adv. Photonics* **5**(3), 036006 (2023).
9. A. Chmyrov et al., "Nanoscopy with more than 100,000 'doughnuts'," *Nat. Methods* **10**(8), 737–740 (2013).
10. N. Zhang et al., "Multiparameter encrypted orbital angular momentum multiplexed holography based on multiramp helico-conical beams," *Adv. Photonics Nexus* **2**(3), 036013 (2023).
11. S. Khonina et al., "The phase rotor filter," *J. Mod. Opt.* **39**(5), 1147–1154 (1992).
12. J. Yan and G. Geloni, "Self-seeded free-electron lasers with orbital angular momentum," *Adv. Photonics Nexus* **2**(3), 036001 (2023).
13. Y. Zang, A. Mirando, and A. Chong, "Spatiotemporal optical vortices with arbitrary orbital angular momentum orientation by astigmatic mode converters," *Nanophotonics* **11**(4), 745–752 (2022).
14. W. Yan et al., "Energy-flow-reversing dynamics in vortex beams: OAM-independent propagation and enhanced resilience," *Optica* **11**(4), 531–541 (2024).
15. A. E. Willner et al., "Design challenges and guidelines for free-space optical communication links using orbital-angular-momentum multiplexing of multiple beams," *J. Opt.* **18**(7), 074014 (2016).
16. G. Xie et al., "Performance metrics and design considerations for a free-space optical orbital-angular-momentum–multiplexed communication link," *Optica* **2**(4), 357–365 (2015).
17. M. Krenn et al., "Communication with spatially modulated light through turbulent air across Vienna," *New J. Phys.* **16**(11), 113028 (2014).
18. M. Krenn et al., "Twisted light transmission over 143 km," *Proc. Natl. Acad. Sci. U. S. A.* **113**(48), 13648–13653 (2016).
19. J. Mendoza-Hernández et al., "Perfect Laguerre–Gauss beams," *Opt. Lett.* **45**(18), 5197–5200 (2020).
20. P. Vaity and L. Rusch, "Perfect vortex beam: Fourier transformation of a Bessel beam," *Opt. Lett.* **40**(4), 597–600 (2015).

21. B. E. A. Saleh and M. C. Teich, *Fundamentals of Photonics*, John Wiley & Sons (2019).
22. R. L. Phillips and L. C. Andrews, "Spot size and divergence for Laguerre Gaussian beams of any order," *Appl. Opt.* **22**(5), 643–644 (1983).
23. A. E. Siegman, "New developments in laser resonators," *Proc. SPIE* **1224**, 2–14 (1990).
24. M. Padgett, "On the focussing of light, as limited by the uncertainty principle," *J. Mod. Opt.* **55**(18), 3083–3089 (2008).
25. A. Bekshaev, K. Y. Bliokh, and M. Soskin, "Internal flows and energy circulation in light beams," *J. Opt.* **13**(5), 053001 (2011).
26. W. Yan et al., "Non-diffracting and self-accelerating Bessel beams with on-demand tailored intensity profiles along arbitrary trajectories," *Opt. Lett.* **46**(7), 1494–1497 (2021).
27. A. Forbes, M. de Oliveira, and M. R. Dennis, "Structured light," *Nat. Photonics* **15**(4), 253–262 (2021).
28. A. Klug, I. Nape, and A. Forbes, "The orbital angular momentum of a turbulent atmosphere and its impact on propagating structured light fields," *New J. Phys.* **23**(9), 093012 (2021).
29. B. B. Yousif and E. E. Elsayed, "Performance enhancement of an orbital-angular-momentum-multiplexed free-space optical link under atmospheric turbulence effects using spatial-mode multiplexing and hybrid diversity based on adaptive MIMO equalization," *IEEE Access* **7**, 84401–84412 (2019).
30. B. B. Yousif, E. E. Elsayed, and M. M. Alzalabani, "Atmospheric turbulence mitigation using spatial mode multiplexing and modified pulse position modulation in hybrid RF/FSO orbital-angular-momentum multiplexed based on MIMO wireless communications system," *Opt. Commun.* **436**, 197–208 (2019).
31. C. E. Shannon, "A mathematical theory of communication," *ACM SIGMOBILE Mob. Comput. Commun. Rev.* **5**(1), 3–55 (2001).
32. L. Hanzo et al., *Quadrature Amplitude Modulation: From Basics to Adaptive Trellis-Coded, Turbo-Equalised and Space-Time Coded OFDM, CDMA and MC-CDMA Systems*, IEEE Press-John Wiley (2004).
33. S. G. Evangelides et al., "Polarization multiplexing with solitons," *J. Lightwave Technol.* **10**(1), 28–35 (1992).
34. B. Mukherjee, *Optical WDM Networks*, Springer Science & Business Media (2006).
35. J. Wang et al., "Terabit free-space data transmission employing orbital angular momentum multiplexing," *Nat. Photonics* **6**(7), 488–496 (2012).
36. N. Bozinovic et al., "Terabit-scale orbital angular momentum mode division multiplexing in fibers," *Science* **340**(6140), 1545–1548 (2013).
37. Z. Wan et al., "Divergence-degenerate spatial multiplexing towards future ultrahigh capacity, low error-rate optical communications," *Light Sci. Appl.* **11**(1), 144 (2022).
38. J. Wang et al., "*N*-dimentional multiplexing link with 1.036-Pbit/s transmission capacity and 112.6-bit/s/Hz spectral efficiency using OFDM-8QAM signals over 368 WDM pol-muxed 26 OAM modes," in *Eur. Conf. Opt. Commun. (ECOC)*, pp. 1–3 (2014).
39. J. Wang et al., "Orbital angular momentum and beyond in free-space optical communications," *Nanophotonics* **11**(4), 645–680 (2022).
40. A. E. Willner et al., "Optical communications using orbital angular momentum beams," *Adv. Opt. Photonics* **7**(1), 66–106 (2015).
41. N. Zhao et al., "Capacity limits of spatially multiplexed free-space communication," *Nat. Photonics* **9**(12), 822–826 (2015).
42. J. Mendoza-Hernández et al., "Laguerre–Gauss beams versus Bessel beams showdown: peer comparison," *Opt. Lett.* **40**, 3739–3742 (2015).
43. R. A. Silverman, *Special Functions and Their Applications*, Courier Corporation (1972).
44. J. D. Schmidt, *Numerical Simulation of Optical Wave Propagation: With Examples in MATLAB*, SPIE Press (2010).

Wenxiang Yan received his BS degree in opto-electronic information science and engineering from the South China University of Technology, China, in 2019. He is currently pursuing a PhD in the National Laboratory of Solid State Microstructures at Nanjing University, under the supervision of Prof. Jianping Ding. His research is mainly focused on the development of structured light and orbital angular momentum with their applications.

Jianping Ding has been a professor in the School of Physics at Nanjing University, China, since 2003. He received his BS and MS degrees in physics from Nanjing University, China, and his PhD in applied physics from Tsukuba University, Japan. His current research interests include light field manipulation, optical information, advanced imaging, and metamaterial.

Biographies of the other authors are not available.